ELSEVIER

Synthetic Metals 138 (2003) 213–221

SYNTHETIC METALS

www.elsevier.com/locate/synmet

Investigation of internal processes in organic light-emitting devices using thin sensing layers

T.A. Beierlein*, B. Ruhstaller, D.J. Gundlach, H. Riel, S. Karg, C. Rost, W. Rieß

IBM Research, Zurich Research Laboratory, Säumerstr. 4, CH-8803 Rüschlikon, Switzerland

Abstract

Systematic studies are a prerequisite for a detailed understanding of the internal processes in organic semiconductors and devices, which is of great importance for optimizing organic light-emitting diode performance. Devices based on small molecules are especially well-suited for introducing thin layers (<10 nm), which in turn can be used as analysis and sensing tools. We use combinatorial methods to fabricate matrices of 10 × 10 individual devices on single substrate in order to ensure reliable and reproducible datasets. We present selected examples to illustrate the strength of this method. These experiments include layer thickness variations in a multilayer system to optimize device performance. A thin metallic and dye-doped sensing layer is inserted into the device to derive the distribution of the electrical field and exciton density, respectively. By means of thickness-dependent photoluminescent measurements we gain insight into luminescence quenching near interfaces.

PACS: 85.60.J; 78.55.Kz; 71.35; 33.50.H

Keywords: Organic LED; Combinatorial method; Sensing layer; Excitation; Quenching

1. Introduction

In recent years, organic light-emitting devices (OLEDs) have made tremendous progress [1,2]. They are now emerging as the leading candidate among the many technologies under development for next-generation flat panel displays. This progress was only possible through systematic device optimization by addressing critical performance issues, such as efficiency, lifetime, and thermal stability [2–5]. Device optimization of OLEDs based on small molecules benefits largely from the ability to tailor the electrical and electro-optical characteristics by the sequential evaporation of multiple layers from various materials. However, as performance depends on a complex interplay between different processes determined by the materials, layer thicknesses, dopant concentrations and electrode configurations, a large parameter space has to be covered for the detailed understanding and optimization of these multilayer devices. Conventional one-by-one device preparation is time-consuming, and the variation of one parameter whilst keeping other factors constant is difficult to achieve. Consequently, reproducibility and comparability are limited when using sequential evaporation runs. Therefore, we chose a combinatorial approach for device fabrication to obtain systematic and reliable datasets. Such data is also a prerequisite for accurate simulations. In the field of OLEDs, this method was introduced first by Schmitz and co-workers for the fabrication of 49 devices on single substrate [6,7]. We developed an ultra-high vacuum (UHV) evaporation system that allows the fabrication of 10 × 10 devices on a single substrate [8]. In addition, the individual devices are electrically isolated and can be fabricated such that each device differs in only one parameter, for example, the thickness of a certain layer. We present selected examples to illustrate the power of this method. These experiments include layer thickness variations in a multilayer system to optimize device performance. A thin metallic and dye-doped sensing layer is inserted into the device to derive the distribution of the electrical field and exciton density, respectively. By means of thickness-dependent photoluminescence (PL) measurements we gain insight into luminescence quenching near interfaces.

2. Experimental

Device fabrication is done in a custom-built evaporation system ‘‘Columbus HPO’’ under UHV conditions. The base

* Corresponding author. Tel.: +41-1-724-8321; fax: +41-1-724-8958.
E-mail address: tib@zurich.ibm.com (T.A. Beierlein).

0379-6779/03/$ – see front matter
doi:10.1016/S0379-6779(02)01269-9

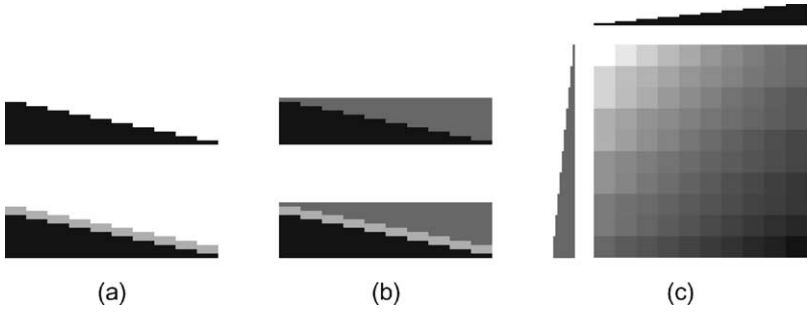

Fig. 1. Examples of possible device configurations: (a) simple staircase and staircase combined with uniform layer for thickness-dependent device series; (b) opposing staircases with/without uniform layer for position-dependent device series; (c) combinatorial matrix consisting of two perpendicular staircase structures.

pressure is less than 10^{-8} mbar and does not exceed 10^{-7} mbar during evaporation of organic materials and metals. The evaporation chamber has 12 effusion cells, which are independently temperature-controlled. Each cell has its own shutter to minimize cross contamination. Four materials can be co-evaporated, therefore even complex doping experiments on multilayer structures can be performed. To increase reproducibility and minimize downtime of the system, evaporation material is refilled or changed via a load lock without venting the main chamber. Deposition rate and thickness are controlled via Leybold Inficon quartz crystal monitors. Typical evaporation rates are of the order of 0.02–1.5 Å/s for dopants and host materials, respectively. The organic layers and the cathode are patterned by different shadow masks, which can be changed in situ. Substrates and shadow masks are transferred via a sample load lock from an argon glove box with less than 1 ppm O_2 and less than 1 ppm H_2O.

The substrates we use are 80 mm × 80 mm glass plates (Corning 1737) cleaned in an ultrasonic bath successively using DI water, acetone and *iso*-propanol. We e-beam evaporate high work function metals such as Pt, Pd, Ir, Mo, and Ni through shadow masks as anodes. The anode pads are arranged in a matrix of 10 × 10 independent devices with an active area of 2 mm × 2 mm each. After deposition of the organic material, a low work function metal—usually Ca or Ca/Mg—is evaporated as semitransparent cathode. During layer deposition the substrate is attached to a rotating sample holder, which has a shutter directly in front of the substrate. The shutter can be moved stepwise during evaporation to allow the deposition of staircase-like films. This enables the fabrication of three types of device series described below.

The basic element of the combinatorial technique is the evaporation of a simple staircase of organic or electrode material (Fig. 1a). Such a step-like film can also be combined with one or more uniform layers. A two-layer structure with two opposing staircases can be deposited when the shutter is rotated 180° after evaporation of the first layer (Fig. 1b) which results, for example, in a two-layer device with constant total device thickness, but with varying positions of the interface between these layers. At the interface a uniform layer, e.g. a doped region, could be introduced. When the shutter is rotated 90° in a two-layer staircase structure all possible thickness combinations are realized (Fig. 1c). From such matrices, systematic and comparable data is obtained for device optimization and further analysis. In addition to these examples, more complex device structures based on different anodes, cathodes and different host/dopant ratios can be fabricated.

In the following sections we show results for the most widely used and investigated OLED configuration based on copper phthalocyanine (CuPc), *N*,*N*′-di(naphtalene-1-yl)-*N*,*N*′-diphenyl-benzidine (NPB) or 2,2′,7,7′-diphenyl-aminospiro-9,9′-bifluorene (STAD), and tris-(8-hydroxyquinolinato)aluminum (Alq_3) [1,5]. In sensing experiments, we used DCJTB [9] as a red emitter.

Good uniformity of the organic layers is mandatory for reliable device comparisons. It is measured on silicon wafers using a Plasmos SD Series Ellipsometer and independently confirmed with profilometry (Tencor alpha-step 200). We achieve a uniformity of the organic layers of better than ±3% over the entire substrate. After OLED fabrication the substrate is unloaded directly into the argon glove box and mounted on an automated *XY*-stage. Each of the 100 devices can be individually addressed, and electrical contact is achieved with a computer-controlled probe head connected to an HP 4145 parameter analyzer. For electroluminescence (EL) intensity measurements the probe head is equipped with a calibrated eye response Si photodiode (LMT GmbH, Berlin, Germany). EL spectra are measured with a spectroradiometer (Photoresearch Spectra Scan 705) via a quartz glass fiber aligned above the sample. In addition, the characterization stage permits the acquisition of PL spectra, transmittance and reflectance measurements, transient EL, and impedance and capacitance–voltage measurements. For PL measurements, a 355 nm laser (NanoUV™, Nanolase) is used as the excitation source. The measurements are taken in reflection mode with a coaxial Y-fiber bundle, where the sample is excited through the outer fibers and the PL signal is detected via the core fibers with the spectroradiometer.

3. Results and discussion

3.1. Two-dimensional layer thickness variations

In order to systematically investigate the influence of layer thickness variations on device performance in multilayer structures a two-layer matrix as shown in Fig. 1c has been fabricated. The devices consist of a constant layer of CuPc (150 Å), and both the NPB and Alq_3 thicknesses are varied from 100 to 1000 Å in steps of 100 Å. Ni is used as anode and Ca 200 Å as a semitransparent cathode for top emission. Fig. 2a and b show the current–voltage (*I–V*) and luminance–voltage (*L–V*) curves of 20 out of 100 devices on a single substrate. Fig. 2a shows 10 devices where the Alq_3 thickness is fixed to 500 Å and the NPB thickness varies from 100 to 1000 Å. Fig. 2b shows 10 devices where the NPB is fixed to 500 Å and the Alq_3 thickness is varied from 100 to 1000 Å.

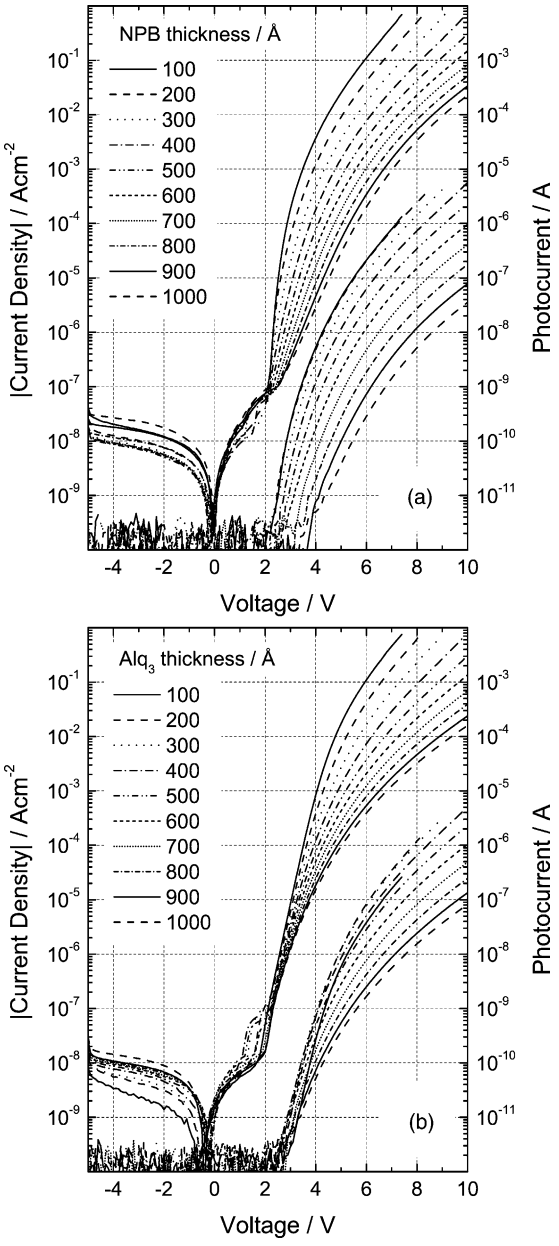

Fig. 2. Current–voltage and luminance–voltage characteristics of 20 out of 100 combinatorial devices consisting of Ni/CuPc/NPB/Alq_3/Ca: (a) NPB thickness varies from 100 to 1000 Å at fixed Alq_3 thickness of 500 Å; (b) Alq_3 thickness varies from 100 to 1000 Å at fixed NPB thickness of 500 Å.

This raw data demonstrates the high quality of the fabrication process. None of the devices show leakage currents, and the rectification ratio is as high as 10^6 at ±5 V. The behavior of all devices in reverse direction and in forward direction up to ≈2 V is basically identical. However, at higher voltages we observe a strong dependence of the current density on the layer thickness for both device series. Here, the OLEDs with varied NPB thickness (Fig. 2a) exhibit a more pronounced thickness dependence than those with Alq_3 variation (Fig. 2b), even at voltages below 4 V. It is self-evident that an increase in device thickness is accompanied by reduced current flow at a certain voltage. However, this greater spreading of the array of *I–V* and *L–V* curves with varied NPB thickness is unexpected. At first glance, the voltage drop across the NPB layer, which has a relatively high hole mobility of $\mu_h \approx 10^{-3}$ $cm^2/(V\,s)$, should be lower than that across the Alq_3 layer with an electron mobility of $\mu_e \approx 10^{-5}$ $cm^2/(V\,s)$ [10]. This straightforward consideration, however, neglects the existence of internal energy barriers for holes at the CuPc/NPB and the NPB/Alq_3 interfaces. Recently, we have shown that it is the interplay between these barriers that controls the current flow and affects the charge balance [11,12]. By increasing the thickness of the NPB layer the electrical field at the CuPc/NPB interface is reduced, leading to reduced hole injection into the NPB layer. As the hole current feeds back on the electron current, the increasing thickness of NPB leads to a significant reduction of the total current.

In the case of fixed NPB and varied Alq_3 thickness (Fig. 2b) the situation is different. Holes injected into NPB accumulate and create a space charge at the NPB/Alq_3 interface. This leads to an enhancement of the field in the Alq_3 layer, which facilitates electron injection from the cathode. The steep increase in current density between 2 and 4 V is similar for all devices, which shows that charge carrier injection is the limiting process in this operating range. At higher voltages the injection is not the only limiting factor, and the divergence of the *I–V* curves reflects the influence of the transport through the materials.

The devices in Fig. 2a and b also show a significant difference in the EL intensity and onset. The pronounced shift of the EL onset, in particular, on devices with varied NPB thickness (Fig. 2b) is due to non-equilibrium effects and can be suppressed by increasing the *I–V* sweep time. In general, the *L–V* signal scales with the *I–V* curves. However, in the case of thin Alq_3 layers (<200 Å) the EL intensity is drastically reduced because of cathode quenching.

The dependence of the driving voltage at constant current density on the individual layer thicknesses can explain the internal field distribution. Fig. 3a shows the voltage

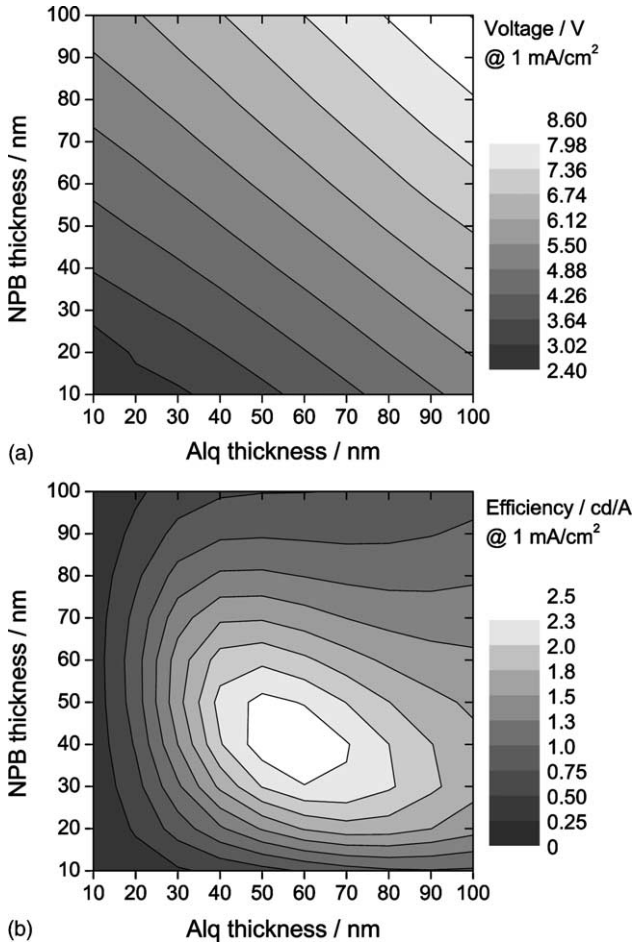

Fig. 3. Two-dimensional grayscale contour maps based on 100 combinatorial devices. The color scheme represents (a) driving voltage at 1 mA/cm^2 and (b) efficiency in cd/A at 1 mA/cm^2 measured through semitransparent Ca cathode.

necessary to drive a current density of 1 mA/cm^2 through the devices as a function of NPB and Alq_3 layer thickness. This two-dimensional representation is based on the measurements of 100 devices. It clearly shows that the operating voltage scales with device thickness. However, a change in NPB layer thickness has an even stronger impact on the operating voltage than the Alq_3 layer in this operating regime.

Another important aspect in device optimization besides minimum operating voltage is the achievement of maximum output efficiency. Fig. 3b shows the efficiency (cd/A) of the combinatorial NPB/Alq_3 matrix devices measured at 1 mA/cm^2. This efficiency map shows a maximum at NPB 40 nm and Alq_3 60 nm with a value of 2.6 cd/A measured through a semitransparent Ca electrode. As mentioned above, the extremely low efficiencies for thin Alq_3 layers point to quenching by the top cathode.

3.2. Potential sensing

As pointed out above, the knowledge of the internal field distribution is essential for a microscopic understanding of device operation. Evidently, the field distribution in a multilayer device is governed by the transport properties of the individual materials and the injection properties controlled by electrodes and internal barriers. The mobilities of charge carriers in organic materials are generally strongly field-dependent. In addition, the process of injection from electrodes or from adjacent organic layers in heterostructures is also determined by the local electric field and accumulated space charges. Various approaches have been used to quantify the internal field distribution in a working OLED.

For example, electroabsorption (EA) measurements have been performed, where the spectral EA responses of the different materials have been associated with the electrical field in the different layers [13,14]. The disadvantage of this technique is that no spatial resolution can be obtained because the extracted field strengths are averaged over the film thickness. Voltage- and frequency-dependent (C–V) measurements provide insight into the electric field distribution of a multilayer stack. Assumptions about the voltage and charge distribution can be made using a proper equivalent circuit consisting of a series circuit of various resistive and capacitive elements [12]. However, this technique can only be used in reverse bias or low forward bias direction before the onset of double carrier injection. As a consequence, the field distribution under real device operation cannot be measured and again only averaged fields can be extracted.

A straightforward method to measure the potential in a device under real operating conditions in reverse and forward bias is direct potential sensing. This method uses a third metal pad sandwiched between the organic layers [15]. As the flexibility of our system allows the insertion of thin layers at various positions in the devices (see Section 2) this approach has been adopted in this work. The schematic device structure is shown from top and side views in Fig. 4. Similar to conventional devices, the area is still 2 mm × 2 mm but a thin metal pad 0.5 mm in width is inserted, which reduces the active device area by 25%. The investigated structure consists of a Ni anode, CuPc (150 Å), STAD (400 Å), Alq_3 (600 Å) and a semitransparent Ca (150 Å)/Mg (50 Å) cathode. The devices are fabricated by staircasing the first layers of the organic stack followed by inserting the third metal sensing pad and finally completing the entire OLED structure (see Fig. 1b, bottom). Recently, Hiramoto et al. [15] demonstrated this method and chose Au as the third pad metal. They therefore had to use a device thicknesses of 8000 Å in total to avoid electrical shorts. In our experiments we use Ca/Mg or Al as intermediate electrodes and succeed in investigating devices with realistic thicknesses of 1100 Å. The sensing pads have a thickness of 100 Å, enabling us to map the potential in ten equidistant steps of 100 Å. For reference, there are ten control devices on the same substrate with identical structure but without the metal sensing layer. The voltage measurements are taken in a three-point configuration with a HP 4145 parameter analyzer. Owing to the high impedance of the SMU ($\geq 10^{12}\,\Omega$)

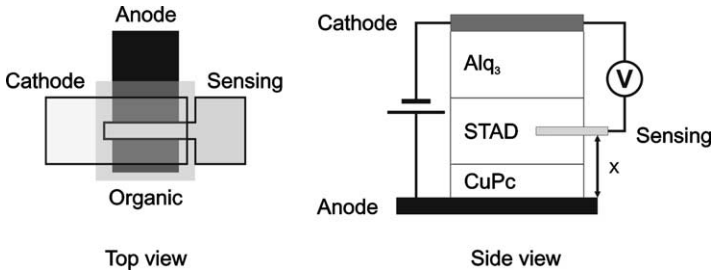

Fig. 4. Schematic structure of a three-terminal device with intermediate electrode. Top view: the third sensing pad covers 25% of the active area of the 2 mm × 2 mm OLED. Side view: the sensing pad is inserted at various positions (x) from the anode into the organic stack.

instrument loading is negligible. In order to exclude non-equilibrium effects the potential of this third pad is measured with reference to both the cathode and the anode. Both sets of devices, i.e. with and without metal pad, show typical I–V characteristics with pronounced diode behavior, i.e. low reverse currents and a sharp increase in the current density at approximately 2.1 V corresponding to double carrier injection. All the devices show a steep characteristic and reach a current density of about 180 mA/cm^2 at 10 V. Fig. 5 shows the measured voltage of the third pad in this CuPc/STAD/Alq_3 OLED plotted versus the pad position. This curve corresponds to the potential distribution in the devices at 9 V. As the cathode is grounded, the potential of anode and cathode corresponds to 9 and 0 V, respectively. A voltage drop of only 0.1 V occurs between the anode and the first metal pad, which is located at the CuPc/STAD interface. The potential difference across the STAD layer is 3.8 V, whereby the larger fraction drops in the first half close to the CuPc layer. Across the Alq_3 layer there is a voltage drop of about 5.1 V. Here, the slope of the potential curve is less steep close to the STAD/Alq_3 interface and becomes steeper towards the cathode. The described trend is generally true for other operating voltages. However, for lower voltages the relative voltage drop over the STAD layer becomes larger than that across the Alq_3 layer.

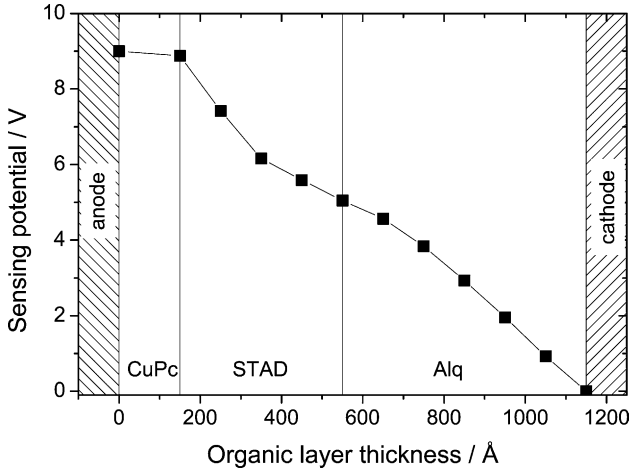

Fig. 5. Sensing potential as a function of sensing layer position in a Ni/CuPc (150 Å)/STAD (400 Å)/Alq_3 (600 Å)/Ca (150 Å)/Mg (50 Å) structure.

The CuPc/STAD and the STAD/Alq_3 interfaces represent energy barriers for holes, whereas electrons have to overcome a barrier from the Alq_3 into the STAD layer. Positive and negative space charges will accumulate at these interfaces during device operation. This process will be further enhanced by the mobility discontinuities of the different materials.

As Ni is a good hole-injecting electrode having a work function of ≈5.2 eV it is assumed to form an Ohmic contact with CuPc. The voltage drop in CuPc is then solely determined by the transport properties and accumulated charges at the CuPc/STAD interface. This interface controls the current flow through the STAD layer and is responsible for the large voltage drop across the STAD layer. As mentioned above, the voltage does not decay linearly with thickness over the STAD layer, which is most likely due to the feedback of accumulated charges at the STAD/Alq_3 interface. Within the spatial resolution of the measurement technique this region of accumulated charges seems to extend more than 200 Å into the STAD layer. On the cathode side no Ohmic contact is achieved by the Ca electrode, particularly at low voltages. In addition, the rather low mobility of electrons in Alq_3 of the order of $\mu_e = 10^{-6}$ cm^2/(V s) [10] leads to a significant voltage drop across the Alq_3 layer. As the STAD/Alq_3 interface prevents electron penetration into STAD the recombination of electrons and holes takes place in the Alq_3 layer. As the hole mobility in Alq_3 is at least one order of magnitude lower than the electron mobility, recombination is restricted to a region close to the STAD interface. Consequently, the voltage drop in this region is lower and can be detected by the potential sensing method (see Fig. 5). The measured potential distribution is consistent with the results on two-dimensional layer variations of the CuPc/NPB/Alq_3 structures (see Section 3.1). This is coherent, because the energy levels as well as the transport properties of STAD and NPB are very similar.

In summary, the described method of potential sensing is used to directly map the potential in an operating organic light-emitting device. In contrast to other methods (EA and C–V), which only measure an averaged electric field over the whole layer, this technique allows a spatial resolution of the electric field distribution. At first glance, the observations are consistent with simple considerations taking energy barriers and space charge accumulation into account.

Nevertheless, the actual potential distribution often depends on peculiarities of the individual device architectures and has therefore to be proved for different organic materials and electrodes to enhance our quantitative understanding.

3.3. PL quenching on thin Alq_3 layers

In Section 3.1 it was mentioned that cathode quenching reduces the quantum efficiency in OLEDs. A further capability of our system is that it provides data of thickness-dependent PL measurements for investigating quenching effects. In general, any interface introduces a perturbation of the intrinsic bulk properties of a material, e.g. in the case of luminescent materials additional non-radiative recombination processes may occur. Surface quenching is one extrinsic mechanism that reduces the efficiency of organic materials and becomes especially important in thin OLED structures when the thickness of the layer is of the order of the diffusion length of the excited state. Metals in particular are known to be efficient quenchers of luminescence because energy can be transferred efficiently and easily dissipated non-radiatively. In the field of OLEDs, quenching has been discussed with regard to experimental and theoretical aspects [16–18]. These quenching processes strongly depend on the distance of the excited state to the quenching site or the interface. In general, quenching is observed when an excited state can act with a quenching center. This can occur either when the excited state is created in close proximity or it can diffuse towards the quenching site within its lifetime.

In order to investigate critical quenching distances, PL measurements are performed on fluorescent thin Alq_3 films on glass in the range from 0 to 2000 Å. The PL signal is measured in reflection mode as described in Section 2. The measured Alq_3 PL spectra are corrected by subtracting the background spectrum of the substrate without Alq_3.

Fig. 6 shows the corrected PL spectra of various Alq_3 thicknesses on glass in a logarithmic representation. All the spectra exhibit the typical Alq_3 emission with the maximum intensity at 530 ± 2 nm and a full width at half maximum (FWHM) of 110 ± 4 nm. The spectra differ only in their intensity, indicating that no thickness-dependent interference effects take place in this sample configuration.

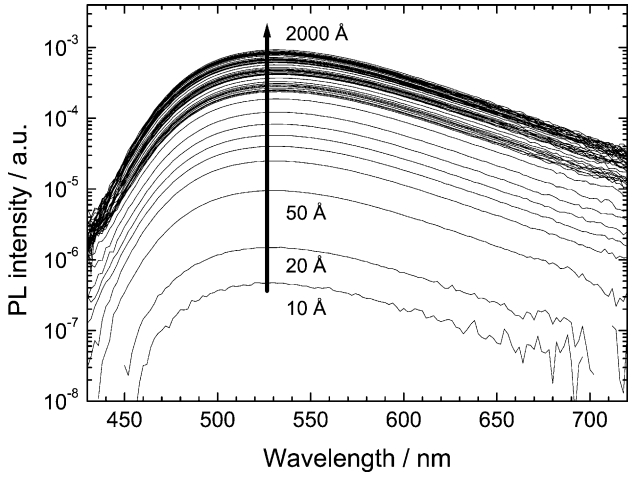

Fig. 6. Photoluminescence spectra of Alq_3 layers with thicknesses from 10 to 2000 Å on glass. No interference effects occur with increasing thickness.

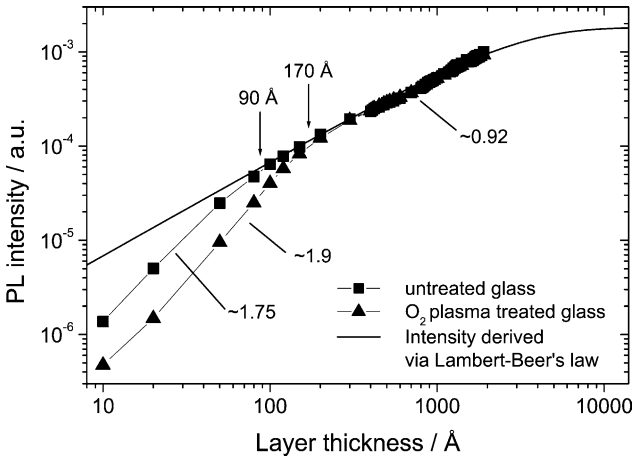

Fig. 7. Photoluminescence intensity of Alq_3 layers on glass as a function of thickness. The deviation from the intensity derived from Lambert–Beer's law is dependent on the substrate treatment, i.e. 90 Å for the untreated and 170 Å for the oxygen plasma-treated substrate.

In Fig. 7, the PL intensities are plotted in a double logarithmic representation as a function of thickness. The plot shows the results on two differently treated substrates: one untreated substrate and one exposed to an oxygen plasma before organic deposition. The PL intensity of both sample series increases monotonically with increasing layer thickness. A simple quantitative description of the PL intensity can be derived with the aid of Lambert–Beer's law (shown as a solid line in Fig. 7). In this PL experiment, the excitation beam is attenuated by optical absorption of the organic molecules in the film. As optical absorption and intrinsic PL quantum efficiency are assumed to be constant for every Alq_3 molecule, the PL intensity I_{PL} is proportional to the absorbed light intensity I_{abs}. The amount of absorbed light I_{abs} as a function of sample thickness d can be derived from Lambert–Beer's law:

$$I_{abs}(d) = I_0(1 - e^{-\alpha d}), \quad (1)$$

where I_0 is the excitation intensity and α the absorption coefficient. This experiment is a relative measurement, and the excitation intensity I_0 and the PL quantum efficiency of Alq_3 need not to be known, because the measured PL intensity I_{PL} is directly proportional to the absorbed intensity I_{abs}. The absorption coefficient α of Alq_3 at 355 nm was determined by ellipsometry $\alpha = 3.8 \times 10^4\ cm^{-1}$. The PL intensity $I_{PL}(d)$ will then saturate for very large thicknesses d, i.e. after $4 \times \alpha^{-1} \approx 1$ μm, 98% of the light is absorbed. This simple description neglects losses due to reflections, waveguiding and interference effects. The intensity calculated from Eq. (1) is drawn as a solid line in Fig. 7. In the

range of 200–2000 Å the experimental data for both substrates agree very well with the predictions of the simple model. Below ≈200 Å we observe deviations of both datasets showing a steeper decay in PL intensity, which suggests the influence of surface quenching. Whereas the samples of the untreated substrate exhibit a slope of ≈1.75 below thicknesses of 90 Å, the samples on the oxygen-treated substrate show a slope of ≈1.9 below 170 Å. As the same Alq_3 is used for both sample series these results hint at an the influence of the different substrate treatments. Oxygen is known to be an efficient luminescence quencher [19], therefore the more pronounced decay in the latter sample series suggests that adsorbed oxygen at the substrate surface acts as an efficient exciton sink. Excitons generated in the organic layer diffuse to the surface and are quenched with a certain probability depending on the substrate treatment. This loss mechanism at the surface feeds back to the actual exciton density and distribution in the thin layer, thus determining the measured PL intensity. The critical quenching distance in this picture is determined by the quenching rate of excitons at the surface and the exciton diffusion length. In a simplified view, the observed critical quenching distances of 90 and 170 Å give an estimate of the diffusion length. An exciton diffusion length in Alq_3 of the order of 200 Å has been estimated by EL experiments [20].

3.4. Delta-doped sensing layer

For optimized OLED architectures it is essential to know the exact location and extent of the recombination and emission zone in the device. The knowledge of energy levels and the charge carrier transport properties can already hint at where emission will take place in the device. However, data about the energy levels and the electron and hole mobilities are often not accurately known. Furthermore, the actual position depends on the details of the organic layer thicknesses and the electrode materials.

An elegant experimental method to determine where recombination and emission in OLEDs take place is to introduce a thin, highly luminescent, dye-doped layer into the host matrix. This sensing layer approach is especially well-suited for small molecule devices as vacuum deposition easily allows the fabrication of multilayer structures with an arbitrary number and sequence of layers. In such a device, the guest molecule emits with a different spectrum from a location exactly determined by the position of this sensing layer. In order to avoid a major disturbance of the electrical device characteristics this sensing layer has to be extremely thin and the dopant concentration rather low. This technique has been used to estimate the exciton profile and diffusion length in Alq_3 [20–22]. However, for an accurate mapping of the emission zone, thin doping layers and numerous reliable samples with finely spaced sensing positions are required.

The structures discussed in this section are fabricated as described in Section 2. A thin layer (25 Å) of Alq_3 doped with DCJTB (≈1%) is inserted into the Alq_3 film at different distances d from the NPB/Alq_3 interface. The OLED structure with the energy levels is sketched in Fig. 8. The devices consist of a Ni anode, CuPc (150 Å), NPB (500 Å), Alq_3 (500 Å) and a semitransparent Ca (200 Å) cathode. The distance d of the doped region from the NPB/Alq_3 interface was varied from 0 to 400 Å, whereby the total thickness of the devices was kept constant.

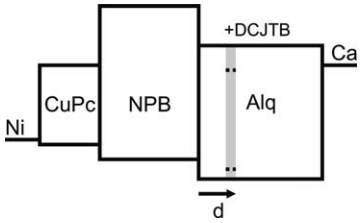

Fig. 8. Schematic energy level diagram of delta-doped devices having a 25 Å Alq_3/DCJTB (1%) sensing layer at various positions (d) in the Alq_3 layer. The device structure is Ni/CuPc (150 Å)/NPB (500 Å)/Alq_3 (500 Å)/Ca (200 Å).

Fig. 9 shows the normalized spectra at a current density of 20 mA/cm^2 as a function of the position in the Alq_3 layer. When placing the DCJTB-doped sensing layer next to the NPB/Alq_3 interface the spectrum exhibits an emission peak at 610 nm and shows a shoulder around 530 nm, which indicates that still some Alq_3 emission (<10%) is present. With increasing distance of the sensing layer from the NPB/Alq_3 interface the relative intensity of the DCJTB emission is reduced and the spectra shift towards almost pure Alq_3 emission. The resulting EL spectra are a superposition of Alq_3 and DCJTB emission. Owing to the large separation of the DCJTB spectrum ($\lambda_{max} = 610$ nm) and Alq_3 emission ($\lambda_{max} = 530$ nm) these spectra can be deconvoluted as shown in Fig. 10. The relative DCJTB intensity is determined by using the spectra of an undoped Alq_3 reference spectrum and the DCJTB emission spectrum. It is observed that the spectral characteristics also depend on the current density. Fig. 11 is a compilation of the relative DCJTB

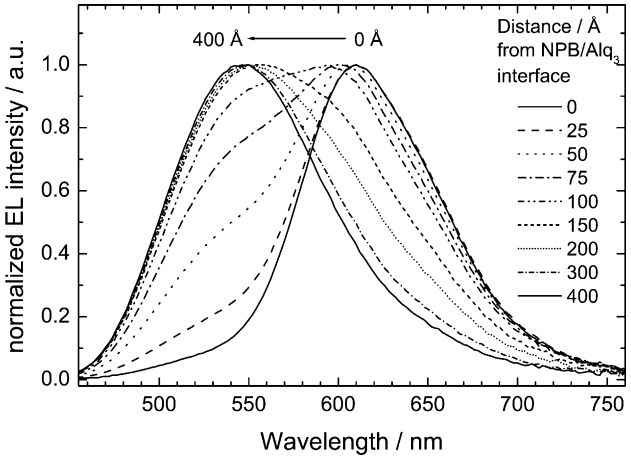

Fig. 9. Normalized EL spectra at 20 mA/cm^2 of delta-doped Alq_3/DCJTB devices having the sensing layer at various positions in the Alq_3 host layer.

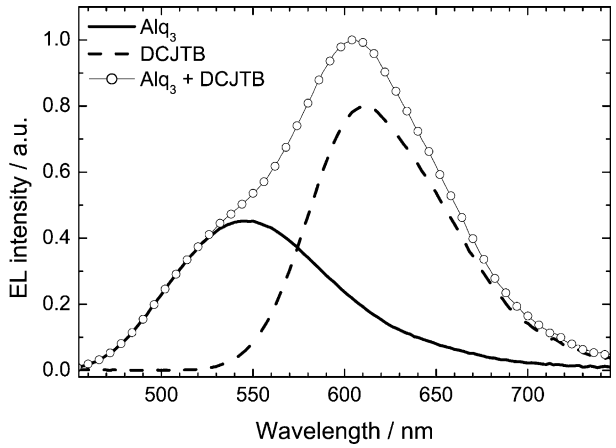

Fig. 10. Deconvolution of measured Alq_3/DCJTB spectra using pure Alq_3 and DCJTB spectra.

emission intensity for all devices measured in the range of 0.01–100 mA/cm^2. When the sensing layer is placed close to the NPB/Alq_3 interface the relative DCJTB emission is almost independent (typically between 90 and 98%) of the current density. With increasing distance from the NPB/Alq_3 interface the fraction of DCJTB emission decreases. In addition, for all devices the relative DCJTB emission decreases with increasing current density, e.g. the relative DCJTB emission of the device whose sensing layer is 100 Å away from the NPB/Alq_3 interface is as high as 68% for 0.01 mA/cm^2, whereas it decreases to only 40% at a current density of 100 mA/cm^2. OLEDs whose sensing layer is 400 Å away from the NPB/Alq_3 interface show DCJTB emission below 4%. As the total Alq_3 layer thickness is 500 Å this low DCJTB emission can additionally be caused by cathode quenching effects (see Section 3.3).

As described above, the emission zone in a CuPc/NPB/Alq_3 structure is located in the Alq_3 close to the NPB/Alq_3 interface. Assuming a constant delta-confined exciton generation at the NPB/Alq_3 interface the steady-state solution of the diffusion equation predicts an exponential decay of the exciton density:

$$S(x) = S(0)\exp\left(-\frac{x}{L}\right), \tag{2}$$

where x represents the distance from the NPB/Alq_3 interface and L the characteristic exciton diffusion length in Alq_3. The emission spectrum of the device with an Alq_3/DCJTB layer of only 25 Å thickness close to the NPB/Alq_3 shows emission of more than 90% originating from DCJTB, indicating that nearly all excitons reaching this sensing layer decay radiatively on the dopant molecules. In Fig. 11 it can be seen that for low current densities, the relative dopant intensity cannot be reasonably represented by an exponential decay, whereas the fit to the experimental data at 100 mA/cm^2 agrees well. From this fit an exciton diffusion length of about 120 Å can be extracted. This number is slightly smaller than the value of 200 Å reported for Alq_3 by Tang et al. [20]. It has to be mentioned that the exciton diffusion length should not depend on the driving conditions. In this experiment, however, the spatial overlap of the distributions of positive and negative charges determines the location of exciton generation. At low current densities the recombination zone is broadened because holes enter the Alq_3 prior to the injection of electrons from the cathode and therefore the assumption of a delta-confined exciton generation zone is not strictly valid. At higher fields, the electron injection and the electron mobility in Alq_3 are drastically increased, thereby confining the exciton generation closer to the NPB layer and justifying a delta-like exciton generation only at higher current densities.

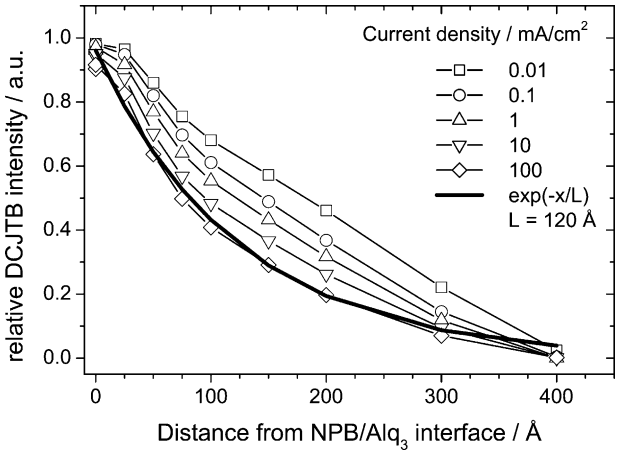

Fig. 11. Relative DCJTB intensity vs. position of the sensing layer for different current densities. An exciton diffusion length of 120 Å can be estimated assuming delta-like exciton generation at the NPB/Alq_3 interface.

4. Summary

We use a UHV evaporation system for combinatorial studies, which allows the simultaneous fabrication of 10×10 individual devices on single substrate. This enables a systematic variation of device parameters such as layer sequence, thickness, and dye-doping position. Several examples demonstrate the versatility of this system. Our results on CuPc/NPB/Alq_3 devices where the thickness of the NPB and Alq_3 layer is varied in two dimensions reveal the importance of the CuPc/NPB interface on the electrical device characteristics. At low voltages the current flow is limited by hole injection controlled by the CuPc/NPB interface, whereas at higher voltages the transport through Alq_3 is limiting. These findings were confirmed by a direct potential-sensing approach using a metal pad inserted into the organic stack to determine the potential distribution in an operating OLED structure. PL experiments on a series of Alq_3 layers with different thicknesses on glass reveal that non-radiative processes reduce the PL efficiency at the glass interface. The critical quenching distance can directly be

measured as a deviation from the PL intensity derived via Lambert–Beer's law. This distance is 90 and 170 Å for an untreated and an oxygen plasma-treated glass substrate, respectively, which indicates different quenching probabilities at these surfaces. Thin delta-doped layers (DCJTB (1%) in Alq_3) can be used to determine the emission zone location and profile in OLED structures. An exciton diffusion length in Alq_3 of the order of 120 Å can be extracted.

In summary, the combinatorial method is a powerful technique to provide reliable and systematic data of complex organic light-emitting structures. These datasets are invaluable for gaining a detailed understanding of the device, for modeling its characteristics, as well as for efficient device optimization.

Acknowledgements

We thank H.-P. Ott, H. Hofmann and M. Tschudy for technical support.

References

[1] C.W. Tang, S.A. Van Slyke, Organic electroluminescent diodes, Appl. Phys. Lett. 51 (12) (1987) 913–915.
[2] M.A. Baldo, D.F. O'Brien, Y. You, A. Shoustikov, S. Sibley, M.E. Thompson, S.R. Forrest, Highly efficient phosphorescent emission from organic electroluminescent devices, Nature 395 (1998) 151–154.
[3] J. Shi, C.W. Tang, Doped organic electroluminescent devices with improved stability, Appl. Phys. Lett. 70 (13) (1997) 1665–1667.
[4] M. Ikai, S. Tokito, Y. Sakamoto, T. Suzuki, Y. Tag, Highly efficient phosphorescence from organic light-emitting devices with an exciton-block layer, Appl. Phys. Lett. 79 (2) (2001) 156–158.
[5] H. Spreitzer, H. Schenk, J. Salbeck, F. Weissoertel, H. Riel, Rieß, Temperature stability of OLEDs using amorphous compounds with spiro-bifluorene core, Proc. SPIE 3797 (1999) 316–324.
[6] C. Schmitz, M. Thelakkat, H.-W. Schmidt, A combinatorial study of the dependence of organic LED characteristics on layer thickness, Adv. Mater. 11 (10) (1999) 821–826.
[7] H.-W. Schmidt, C. Schmitz, P. Pösch, M. Thelakkat, Combinatorial methods for screening and optimization of materials and device parameters in organic light-emitting diodes, Proc. SPIE 3797 (1999) 58–65.
[8] T.A. Beierlein, H.-P. Ott, H. Hofmann, H. Riel, B. Ruhstaller, B. Crone, S. Karg, W. Rieß, Combinatorial device fabrication and optimization of multilayer organic LEDs, Proc. SPIE 4464 (2002) 178–186.
[9] C.H. Chen, C.W. Tang, J. Shi, K.P. Klubek, Improved red dopants for organic electroluminescent devices, Macromol. Symp. 125 (1997) 49–58.
[10] S. Barth, P. Müller, H. Riel, P.F. Seidler, W. Rieß, H. Vestweber, H. Bässler, Electron mobility in tris-(8-hydroxyquinoline)aluminum thin films determined via transient electroluminescence from single- and multilayer organic light-emitting diodes, J. Appl. Phys. 89 (7) (2001) 3711–3719.
[11] W. Rieß, H. Riel, T. Beierlein, W. Brütting, P. Müller, P.F. Seidler, Influence of trapped and interfacial charges in organic multilayer light-emitting devices, IBM J. Res. Dev. 45 (1) (2001) 1–13.
[12] H. Riel, T.A. Beierlein, S. Karg, W. Rieß, The role of copper phthalocyanine in multilayer organic LEDs based on small molecules, Proc. SPIE 4800, 2003, in press.
[13] I.H. Cambell, M.D. Joswick, I.D. Parker, Direct measurement of the internal electric field distribution in a multilayer organic light-emitting diode, Appl. Phys. Lett. 67 (21) (1995) 3171–3173.
[14] F. Rohlfing, T. Yamada, T. Tsutsui, Electroabsorption spectroscopy on tris-(8-hydroxyquinoline)aluminum-based light-emitting diodes, J. Appl. Phys. 86 (9) (1999) 4978–4984.
[15] M. Hiramoto, K. Koyama, K. Nakayama, M. Yokoyama, Direct measurement of internal potential distribution in organic electroluminescent diodes during operation, Appl. Phys. Lett. 76 (10) (2000) 1336–1338.
[16] R.R. Chance, A. Prock, R. Silbey, Molecular fluorescence and energy transfer near interfaces, Adv. Chem. Phys. 37 (1978) 1–65.
[17] V.-E. Choong, Y. Park, Y. Gao, M.G. Mason, C.W. Tang, Photoluminescence quenching of Alq_3 by metal deposition: a surface analytical investigation, J. Vac. Sci. Technol. A 16 (3) (1998) 1838–1841.
[18] A.L. Burin, M.A. Ratner, Exciton migration and cathode quenching in organic light-emitting diodes, J. Phys. Chem. A 104 (2000) 4704–4710.
[19] J.B. Birks, Photophysics of Aromatic Molecules, Wiley/Interscience, New York, 1970.
[20] C.W. Tang, S.A. Van Slyke, C.H. Chen, Electroluminescence of doped organic thin films, J. Appl. Phys. 65 (9) (1989) 3610–3616.
[21] T. Mori, T. Mizutani, Application of energy transfer model to partially DCM-doped Alq_3 light-emitting diode, Polym. Adv. Technol. 8 (1997) 471–476.
[22] J. Lam, T.C. Gorjanc, Y. Tao, M. D'Iorio, Selective doping of multilayer organic light-emitting devices, J. Vac. Sci. Technol. A 18 (2) (2000) 593–596.